Highly Crystalline Multimetallic Nanoframes with Three-Dimensional Electrocatalytic Surfaces

Chen Chen,†[1,2,3] Yijin Kang†[4], Ziyang Huo,[1,2] Zhongwei Zhu,[1,2] Wenyu Huang,[1] Huolin Xin,[2] Joshua D. Snyder[4], Dongguo Li[4], Jeffrey A. Herron[5], Manos Mavrikakis[5], Miaofang Chi[6], Karren L. More[6], Yadong Li,[3] Nenad M. Markovic[4], Gabor A. Somorjai,[1,2] Peidong Yang*[1,2,7,8], Vojislav R. Stamenkovic*[4]

Affiliations:

[1] Department of Chemistry, University of California, Berkeley, California 94720, USA.

[2] Materials Sciences Division, Lawrence Berkeley National Laboratory, Berkeley, California 94720, USA.

[3] Department of Chemistry, Tsinghua University, Beijing 100084, P. R China.

[4] Materials Science Division, Argonne National Laboratory, Argonne, Illinois, 60439, USA.

[5] Department of Chemical and Biological Engineering, University of Wisconsin, Madison, Wisconsin, 53706, USA.

[6] Division of Material Science and Technology, Oak Ridge National Laboratory, Oak Ridge, Tennessee 37831, USA.

[7] Department of Chemistry, Faculty of Science, King Abdulaziz University, Jeddah 21589, P.O. Box 80203, Saudi Arabia

[8] Kavli Energy NanoSciences Institute at the University of California, Berkeley and the Lawrence Berkeley National Laboratory

† These authors contributed equally to this work.

*Corresponding author. E-mail: p_yang@berkeley.edu (P.Y.); vrstamenkovic@anl.gov (V.R.S.)

Control of structure at the atomic level can precisely and effectively tune catalytic properties of materials, enabling enhancement in both activity and durability. We report synthesis of a highly active and durable class of electrocatalysts by exploiting the structural evolution of Pt-Ni bimetallic nanocrystals. The starting material, crystalline $PtNi_3$ polyhedra, transformed in solution by interior erosion into Pt_3Ni nanoframes with surfaces that have three-dimensional molecular accessibility. The edges of these $PtNi_3$ polyhedra, which were Pt rich, are maintained in the final Pt_3Ni nanoframes. Both the interior and exterior catalytic surfaces of this open framework structure are composed of the nano-segregated Pt-Skin structure that exhibits enhanced oxygen reduction reaction (ORR) activity. The Pt_3Ni nanoframe catalysts achieved over 36 and 22-fold enhancement in mass and specific activities, respectively, for this reaction versus ORR in comparison to state-of-the-art Pt/C catalysts during prolonged exposure to reaction conditions.

Platinum (Pt) is a highly efficient electrocatalyst for both the cathodic oxygen reduction reaction (ORR) in fuel cells (and metal-air batteries) and the hydrogen evolution reaction (HER) in alkaline electrolyzers (*1-20*). However, the high cost and scarcity of Pt are key obstacles for its broad deployment in fuel cells and metal-air batteries for both stationary and portable applications. Intense research efforts have been focused on developing high-performance electrocatalysts with minimal precious metal content and cost (*1-17*). Specifically, alloying Pt with non-noble metals can reduce the Pt content of electrocatalysts by increasing their intrinsic activity (*1-13*). We demonstrated that the formation of a nano-segregated Pt(111)-Skin structure over a bulk single-crystal Pt_3Ni alloy enhanced the ORR activity by two orders of magnitude (vs. Pt/C) through altered electronic structure of Pt surface atoms (*1*). However, these materials cannot be easily integrated into electrochemical devices but their outstanding catalytic performance needs to be mimicked in nanoparticulate materials that offer high surface areas. Caged, hollow or porous nanoparticles offer a promising approach to meeting these performance goals. The hollow interior diminishes buried non-functional precious metal atoms, and their uncommon geometry provides a pathway for tailoring physical and chemical properties. They have thus attracted increasing interest in the fields of catalysis, biomedical materials, electronics, etc. (*5-7, 20-28*).

Hollow nanostructures have been prepared by template-directed protocol relying on the removal of micro-/nano-beads, treatments based on the Kirkendall effect, the galvanic displacement reaction, or both (*20-29*). In this report, we present a novel class of electrocatalysts exploiting structural evolution of bimetallic nanoparticles during which

$PtNi_3$ solid polyhedra were transformed into hollow Pt_3Ni nanoframes with surfaces that have three-dimensional (3D) molecular accessibility. Controlled thermal treatment of the resulting nanoframes formed the desired Pt-Skin surface structure (*1, 9*). Synthesis of Pt_3Ni nanoframes can be readily scaled up to produce high-performance electrocatalysts at gram-scale, and importantly our protocol can be generalized toward the design of other multimetallic nanoframe systems.

We synthesized $PtNi_3$ polyhedra in oleylamine that had a uniform rhombic dodecahedron morphology and size (20.1 ± 1.9 nm), as observed along three representative zone axes [Fig. 1A and 2A, figure S1 and S2 (see Supporting Online Materials)]. The oleylamine-capped $PtNi_3$ polyhedra were dispersed in nonpolar solvents such as hexane and chloroform and kept under ambient conditions for 2 weeks, during which time they transformed into Pt_3Ni nanoframes [Fig. 1 and figure S3 (see Supporting Online Materials)], with unchanged symmetry and size [Fig. 1 and 2, and figure S4 (see Supporting Online Materials)]. Increasing the solution temperature to 120 °C decreased the time needed for this morphological evolution to 12 hours [figure S5 (see Supporting Online Materials)]. These conditions were used to trace the entire structural and compositional evolution process at 2-hr time intervals [figure S6 (see Supporting Online Materials)]. Samples at three representative stages (0, 6, 12 hours) were examined by transmission electron microscopy (TEM) (Fig. 1, A to C). The initially solid nanostructures gradually eroded into hollow frames, and the bulk composition changed from $PtNi_3$ to PtNi and eventually Pt_3Ni, as evidenced by x-ray diffraction (XRD) patterns and energy-dispersive x-ray (EDX) spectra [figure S7 (see Supporting Online

Materials)]: all three samples are face-centered cubic (fcc) and the three main XRD peaks for each sample, namely, (111), (200) and (220), are located between those for Pt and Ni; during the evolution process, the peaks shifted towards lower angle (increased d-spacing), suggesting that the nanostructures have changed from Ni-rich to Pt-rich alloys, in accord with the EDX results. After dispersion of nanoframes onto a high surface area carbon support (Vulcan XC-72) and subsequent thermal treatment in inert gas (Ar) atmosphere between 370 and 400 °C, most nanoframes developed the smooth Pt-Skin type of structure (Fig. 1D).

High-resolution TEM (HRTEM) and high-angle annular dark-field scanning transmission electron microscopy (HAADF-STEM) showed that the initial $PtNi_3$ polyhedra were fcc nanocrystals (Fig. 2). For the hollow Pt_3Ni nanoframes, the HAADF-STEM images showed an architecture consisting of 24 edges (ca. 2 nm in diameter) of the parent rhombic dodecahedron (Fig. 2B) that maintained the single-crystalline structure [figure S8 (see Supporting Online Materials)].

In contrast to other synthesis procedures for hollow nanostructures that involve corrosion induced by harsh oxidizing agents or applied potential, the method described here proceeds spontaneously in air through free corrosion. We followed the compositional evolution of these framed, bimetallic nanostructures with x-ray photoelectron spectroscopy (XPS). In the presence of dissolved oxygen, the surface Ni atoms are more susceptible to being oxidized than Pt atoms. The Ni 2p and Pt 4f XPS spectra of $PtNi_3$ polyhedra obtained in vacuum (Al Kα, $h\nu$ = 1486.6 eV) show that the majority of the

surface Ni was oxidized and the surface Pt was mainly in the metallic state (Fig. 2, D and E). Oxidized Ni can readily form soluble metal complexes with the oleylamine ligands (*30*) and lead to a higher dissolution rate for Ni versus Pt that drives compositional change from Ni-rich to Pt-rich, until the stable Pt_3Ni phase (*31*) is formed. The intensity of Pt^{2+} with respect to Pt was barely altered after the system evolved into the final stage (Fig. 2, D and E), whereas the ratio of Ni^{x+} at the surface decreased substantially, implying that oxidation of Ni on the surface became more difficult in the stable Pt_3Ni composition. Additionally, we carried out in-situ ambient-pressure XPS studies to examine the changes in surface chemistry of both $PtNi_3$ and Pt_3Ni in response to the different exposure atmospheres (*32*), the results of which support the mechanism proposed above (for details, see Supporting Online Materials, figure S10).

The corresponding morphological changes of the solid polyhedral particles occurred through preferential dissolution in the interior of the polyhedral faces, rather than on the edges, driven by an inhomogeneous elemental distribution in the initial nanostructure revealed by TEM (Fig. 1 and 2). The contour of frames could be imaged immediately after synthesis because of the higher Pt content on the edges. EDX elemental mapping (Fig. 2C) and site-specific EDX analyses [figure S11 (see Supporting Online Materials)] for the $PtNi_3$ polyhedra showed that Ni exhibited a relatively homogeneous distribution inside of the particles, but Pt was relatively concentrated at the edges. Such elemental distribution in the original solid polyhedra could be caused by preferential etching of low coordinated Ni along the edges because of the presence of trace oxygen in the solution during the initial nanoparticle synthesis. During the evolution process to form the nanoframes this leads to stable Pt_3Ni composition on the edges (Fig. 2C), as both Pt and

Ni species dissolved from the interior of the polyhedra. Taken together, the inhomogeneous distribution of Pt and the high dissolution rate of Ni create hollow Pt_3Ni nanoframes containing 24, 2-nm diameter edges that retain the high crystallinity of the parent structure [figure S8 (see Supporting Online Materials)].

The electrocatalytic properties of Pt_3Ni nanoframes were evaluated and compared to PtNi/C and commercial state-of-the-art Pt/C nanoscale electrocatalysts (Fig. 3). The polarization curves shown in Fig. 3B show an increase in ORR activity in the following order: Pt/C < PtNi/C << Pt_3Ni nanoframes. As seen in the Tafel plot (Fig. 3C), Pt_3Ni nanoframes exhibited substantially higher activity, with a slope of 46 mV dec^{-1} compared to that of 73 mV dec^{-1} for Pt/C, which is in agreement with that of $Pt_3Ni(111)$-Pt-Skin (*3*). The kinetic current densities representing the intrinsic activities were calculated by the Koutecky-Levich equation and summarized in Fig. 3, E and F, as specific and mass activities, respectively. The specific activities were calculated through normalization by the electrochemically active surface area (ECSA) as estimated by CO-stripping (electrooxidation of adsorbed CO).

The ratio between ECSA values determined by integrated charge from CO-stripping and underpotentially deposited hydrogen (H_{upd}) was 1.52 for the Pt_3Ni nanoframes, strongly suggesting formation of a Pt-Skin terminated (111)-like surface structure [table S1 (see Supporting Online Materials), Fig. 3A] (*4*). Moreover, EDX line profiles confirmed the presence of Pt-Skin on the nanoframe surfaces with a thickness of at least two Pt monolayers (MLs) [figure S13 (see Supporting Online Materials)]. As a result, the specific activity of Pt_3Ni nanoframes at 0.95 V exhibited an improvement factor of over

16 versus commercial Pt/C electrocatalyst (Fig. 3E). The extraordinarily high activity of the Pt_3Ni nanoframes combined with the distinct ratio between $ECSA_{CO}/ECSA_{Hupd}$ and EDX line profile is indicative of a Pt_3Ni-Pt-Skin formation, however, with a top most Pt-Skin thickness of at least 2 MLs rather than 1 ML, which is common for ideal bulk $Pt_3Ni(111)$ single crystal. In spite of that divergence, 2 MLs of Pt-Skin indeed sustain the enhancement in the ORR rate that is based on altered electronic structure of Pt topmost atoms by subsurface Ni, causing a lower surface coverage of spectator species, namely OH_{ad}, and hence superior catalytic properties (*1*).

Surface strain of the Pt atoms also contributes to the functional properties of the nanoframes. The influence of strain on catalytic behavior was evaluated by density functional theory (DFT) simulations in which dependence of activity vs. Pt-Skin thickness was estimated to be optimal for 2 to 3 MLs (see Supporting Online Materials, figure S15). These findings have a pivotal role not only in understanding the origin of the high catalytic activity, but also reflect on durability of the catalyst. The Pt-Skin surface structure of the nanoframes in conjunction with their high ECSA provides the link between well-defined extended surfaces and highly crystalline nanoscale electrocatalysts. The synergy between specific activity and the open architecture of the Pt_3Ni nanoframes that enables access of reactants to both the internal and external surfaces [figure S16 (see Supporting Online Materials)] led to an unprecedented 22-fold enhancement in the mass activity vs. Pt/C (Fig. 3F). The mass activity calculated at 0.9 V (5.7 A $mg^{-1}Pt$) is over one order of magnitude higher than the US Department of Energy's 2017 target (0.44 A $mg^{-1}Pt$), making the Pt_3Ni nanoframes the most efficient electrocatalyst for the ORR.

In addition to the high intrinsic and mass activities, the Pt_3Ni nanoframes exhibited remarkable durability throughout electrochemical operation. We cycled the potential between 0.6 V and 1.0 V for a duration of 10,000 cycles at different sweep rates between 2-200 mV s^{-1}. For the state-of-the-art Pt/C electrocatalysts, such cycles cause substantial loss of specific surface area (c.a. 40%) because of dissolution of Pt surface atoms and agglomeration of Pt particles through surface oxidation/reduction processes (*8, 19*). In contrast, STEM (dark field and bright field) images confirmed that the frame structure was preserved while activity loss was negligible after 10,000 potential cycles (Fig. 4). The enhanced durability is ascribed to the electronic structure of the Pt-Skin surface resulting in a lower coverage of oxygenated intermediates because of the weaker oxygen binding strength, which diminishes the probability of Pt dissolution (*1*). In addition, the optimized Pt-Skin thickness of at least 2 MLs hinders the loss of subsurface transition metal through the place-exchange mechanism during electrochemical operation consequently preserving the high intrinsic activity (*9*). The Pt_3Ni nanoframe structure was retained after annealing at 400°C in Ar for several hours, demonstrating its thermal stability [figure S19 (see Supporting Online Materials)].

As reported by Erlebacher and co-workers, protic ionic liquids (IL) can be integrated into a nanoporous catalyst, where the high O_2 solubility of IL increases the O_2 concentration at the catalyst surface, resulting in higher attempt frequencies for the ORR and consequently higher activity (*5, 6*). We used [MTBD][NTf_2] [figure S20 (see Supporting Online Materials)], an ionic-liquid that has an O_2 solubility ($C_{O2,[MTBD][NTf2]}$ = 2.28 ± 0.12 mM) approximately twice that of the common electrolyte $HClO_4$ ($C_{O2,HClO4}$ = 1.21 mM (*6*), see Supporting Online Materials). Capillary forces exerted by the Pt_3Ni nanoframes

pulled the IL inside the frames and prevented it from being washed away by electrolyte [Fig. 3A, figure S21 to S23 (see Supporting Online Materials)]. The IL-encapsulated Pt_3Ni nanoframes showed sustained superior activity upon prolonged (10,000) potential cycling without noticeable decay in performance, reinforcing that the frame architecture is a desired morphology to fully exploit the beneficial properties of ILs [figure S24 (see Supporting Online Materials)]. The IL-encapsulated Pt_3Ni nanoframes exhibited a 36-fold enhancement in mass activity and 22-fold enhancement in specific activity compared with Pt/C.

We also applied these electrocatalysts to the hydrogen evolution reaction (HER), which is the crucial cathodic reaction in water-alkali electrolyzers. Recently, it has been demonstrated that electrochemically deposited $Ni(OH)_2$ clusters on Pt surfaces can facilitate dissociation of water, thus increase the HER activity *(15)*. In the case of highly crystalline Pt_3Ni-Pt-Skin nanoframe surfaces modified by electrochemically deposited $Ni(OH)_2$ clusters [Fig. 3D, figure S25 (see Supporting Online Materials)], the HER activity was enhanced by almost one order-of-magnitude compared to Pt/C. This result further emphasizes the beneficial effects of the open architecture and surface compositional profile of the Pt_3Ni nanoframes in electrocatalysis.

The open structure of the Pt_3Ni nanoframes address some of the major design criteria for advanced nanoscale electrocatalysts, namely, high surface-to-volume ratio, 3D surface molecular accessibility, and optimal precious metal utilization. The approach presented here for the structural evolution of a bimetallic nanostructure from solid polyhedra to hollow highly crystalline nanoframes with controlled size, structure and composition can

be readily applied to other multimetallic electrocatalysts such as PtCo, PtCu, Pt/Rh-Ni, and Pt/Pd-Ni [figure S26 to S29 (see Supporting Online Materials)].

References and Notes:

1 V. R. Stamenkovic, *et al.,* Improved oxygen reduction activity on $Pt_3Ni(111)$ via increased surface site availability. *Science* **315**, 493-497 (2007).

2 S. Guo, S. Zhang, S. Sun, Tuning nanoparticle catalysis for the oxygen reduction reaction. *Angew. Chem. Int. Ed.* **52**, 8526-8544 (2013).

3 D. F. Van Der Vliet, *et al.,* Mesostructured thin films as electrocatalysts with tunable composition and surface morphology. *Nat. Mater.* **11**, 1051-1058 (2012).

4 D. F. Van Der Vliet, *et al.,* Unique electrochemical adsorption properties of Pt-Skin surfaces. *Angew. Chem. Int. Ed.* **51**, 3193-3196 (2012).

5 J. Snyder, K. Livi, J. Erlebacher, Oxygen reduction reaction performance of [MTBD][beti]-encapsulated nanoporous NiPt alloy nanoparticles. *Adv. Funct. Mater.* **23**, 5494-5501 (2013).

6 J. D. Snyder, T. Fujita, M. W. Chen, J. Erlebacher, Oxygen reduction in nanoporous metal-ionic liquid composite electrocatalysts. *Nat. Mater.* **9**, 904-907 (2010).

7 J. Erlebacher, M. J. Aziz, A. Karma, N. Dimitrov, K. Sieradzki, Evolution of nanoporosity in dealloying. *Nature* **410**, 450-453 (2001).

8 P. J. Ferreira, *et al.*, Instability of Pt/C electrocatalysts in proton exchange membrane fuel cells - A mechanistic investigation. *J. Electrochem. Soc.* **152**, A2256-A2271 (2005).

9 C. Wang, *et al.,* Design and synthesis of bimetallic electrocatalyst with multilayered Pt-Skin surfaces. *J. Am. Chem. Soc.* **133**, 14396-14403 (2011).

10 D. Wang, *et al.*, Structurally ordered intermetallic platinum-cobalt core-shell nanoparticles with enhanced activity and stability as oxygen reduction electrocatalysts. *Nat. Mater.* **12**, 81-87 (2013).

11 J. Zhang, H. Z. Yang, J. Y. Fang, S. Z. Zou, Synthesis and oxygen reduction activity of shape-controlled Pt_3Ni nanopolyhedra. *Nano Lett.* **10**, 638-644 (2010).

12 J. Wu, *et al.,* Truncated octahedral Pt_3Ni oxygen reduction reaction electrocatalysts. *J. Am. Chem. Soc.* **132**, 4984-4985 (2010).

13 C. H. Cui, L. Gan, M. Heggen, S. Rudi, P. Strasser, Compositional segregation in shaped Pt alloy nanoparticles and their structural behaviour during electrocatalysis, *Nat. Mater.* **12**, 765-771 (2013)

14 C. Wang, *et al.*, Synthesis of monodisperse Pt nanocubes and their enhanced catalysis for oxygen reduction. *J. Am. Chem. Soc.* **129**, 6974-6975 (2007).

15 R. Subbaraman, *et al.,* Enhancing hydrogen evolution activity in water splitting by tailoring Li^+-Ni(OH)(2)-Pt interfaces. *Science* **334**, 1256-1260 (2011).

16 Y. Liu, D. Gokcen, U. Bertocci, T. P. Moffat, Self-terminating growth of platinum films by electrochemical deposition. *Science* **338**, 1327-1330 (2012).

17 Y. J. Kang, *et al.,* Heterogeneous catalysts need not be so "heterogeneous": monodisperse Pt nanocrystals by combining shape-controlled synthesis and purification by colloidal recrystallization. *J. Am. Chem. Soc.* **135**, 2741-2747 (2013).

18 M. Cargnello, *et al.,* Control of metal nanocrystal size reveals metal-support interface role for ceria catalysts. *Science* **341**, 771-773 (2013).

19 L. Tang, *et al.,* Electrochemical stability of nanometer-scale Pt particles in acidic environments. *J. Am. Chem. Soc.* **132**, 596-600 (2010).

20 Y. D. Yin, *et al.* Formation of hollow nanocrystals through the nanoscale Kirkendall Effect. *Science* **304**, 711-714 (2004).

21 J. E. Macdonald, *et al.,* Hybrid nanoscale inorganic cages. *Nat. Mater.* **9**, 810-815 (2010).

22 S. E. Skrabalak, *et al.* Gold nanocages: synthesis, properties, and applications. *Acc. Chem. Res.* **41**, 1587-1595 (2008).

23 M. McEachran, *et al.* Ultrathin gold nanoframes through surfactant-free templating of faceted pentagonal silver nanoparticles. *J. Am. Chem. Soc.* **133**, 8066-8069 (2011).

24 X. Wang, *et al.* One-pot solution synthesis of cubic cobalt nanoskeletons. *Adv. Mater.* **21**, 1636-1640 (2009).

25 M. E. Davis, Ordered porous materials for emerging applications. *Nature* **417**, 813-821 (2002).

26 S. A. Johnson, P. J. Ollivier, T. E. Mallouk, Ordered mesoporous polymers of tunable pore size from colloidal silica templates. *Science* **283**, 963-965 (1999).

27 M. S. Yavuz, *et al.,* Gold nanocages covered by smart polymers for controlled release with near-infrared light. *Nat. Mater.* **8**, 935-939 (2009).

28 M. A. Mahmoud, W. Qian, M. A. El-Sayed, Following charge separation on the nanoscale in Cu_2O-Au nanoframe hollow nanoparticles. *Nano Lett.* **11**, 3285-3289 (2011).

29 M. H. Oh, *et al.,* Galvanic replacement reactions in metal oxide nanocrystals. *Science* **340**, 964-968 (2013).

30 D. Wang, Y. D. Li, Effective octadecylamine system for nanocrystal synthesis. *Inorg. Chem.* **50**, 5196 (2011).

31 C. E. Dahmani, M. C. Cadeville, J. M. Sanchez, J. I. Moranlopez, Ni-Pt phase diagram: experiment and theory. *Phys. Rev. Lett.* **55**, 1208 (1985).

32 F. Tao, *et al.*, Reaction-driven restructuring of Rh-Pd and Pt-Pd core-shell nanoparticles. *Science.* **322**, 932-934 (2008).

33 B. Hammer, L. B. Hansen, J. K. Norskov, Improved adsorption energetics within density-functional theory using revised Perdew-Burke-Ernzerhof functionals. *Phys. Rev. B* **59**, 7413-7421 (1999).

34 J. Greeley, J. K. Norskov, M. Mavrikakis, Electronic structure and catalysis on metal surfaces. *Annu. Rev. Phys. Chem.* **53**, 319-348 (2002).

35 D. J. Chadi, M. L. Cohen, Special points in the Brillouin zone. *Phys. Rev. B* **8**, 5747-5753 (1973).

36 D. Vanderbilt, Soft self-consistent Pseudopotentials in a generalized Eigenvalue formalism. *Phys. Rev. B* **41**, 7892-7895 (1990).

37 J. P. Perdew, Atoms, molecules, solids, and surfaces – applications of the generalized gradient approximation for excange and correlation. *Phys. Rev. B* **46**, 6671-6687 (1992).

38 J. A. White, D. M. Bird, Implementation of gradient-corrected exchange-correlation potentials in Car-Parrinello total-energy calculations. *Phys. Rev. B* **50**, 4954-4957 (1994).

39 J. A. Herron, J. Jiao, K. Hahn, G. Peng, R. R. Adzic, Oxygen reduction reaction on platinum-terminated "onion-structured" alloy catalysts. *Electrocatal.* **3**, 192-202 (2012).

40 Y. J. Kang, *et al*., Shape-controlled synthesis of Pt nanocrystals: the role of metal carbonyls. *ACS Nano* **7**, 645-653 (2013).

Acknowledgments:

The research conducted at Lawrence Berkeley National Laboratory and Argonne National Laboratory, was supported by the U.S. Department of Energy, Office of Science, Office of Basic Energy Sciences, Materials Sciences and Engineering Division, under Contract No. DE-AC02-05CH11231 and No. DE-AC02-06CH11357, respectively. The portion of work related to catalyst durability was supported by the Office of Energy Efficiency and Renewable Energy, Fuel Cell Technologies Program. The work related to nanoparticle catalysis at Berkeley was supported by KAU. Work at University of Wisconsin was supported by U.S. Department of Energy, Office of Science, Office of Basic Energy Sciences, under Contract No. DE-FG02-05ER15731 and computations were performed at supercomputing centers located at NERSC, PNNL, and ANL, all supported by U.S. Department of Energy. Microscopy studies were accomplished at the Center for Nanophase Materials Sciences at Oak Ridge National Laboratory, which is sponsored by the Scientific User Facilities Division, Office of Basic Energy Sciences, U.S. Department of Energy and at the Electron Microscopy Center (ANL). We thank S. Alayoglu for carrying out the site-specific EDX on the alloy nanostructures and Z. Liu for help on XPS analysis.

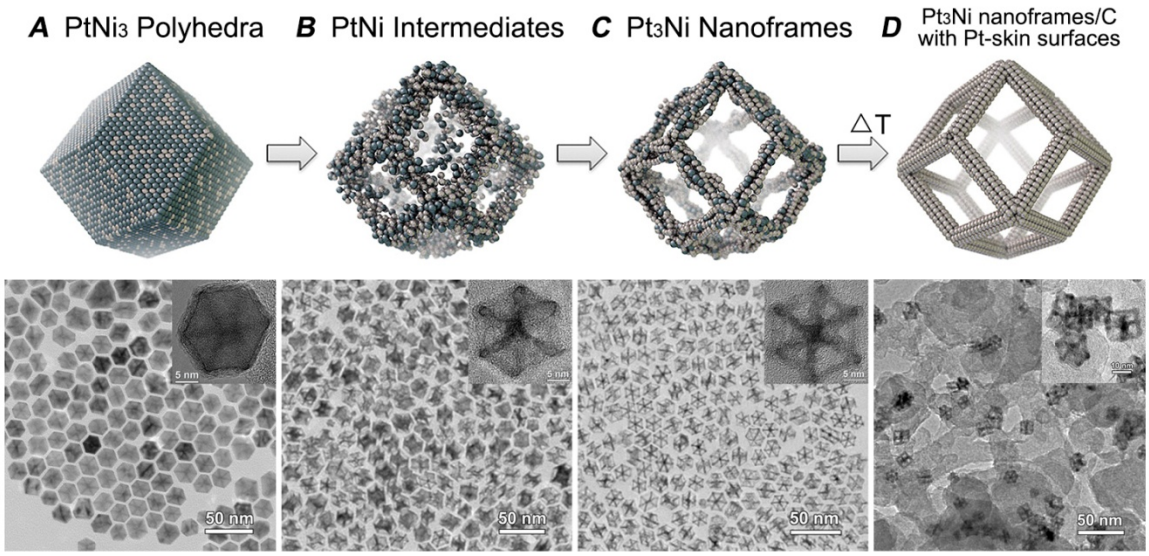
A PtNi3 Polyhedra
B PtNi Intermediates
C Pt3Ni Nanoframes
D Pt3Ni nanoframes/C with Pt-skin surfaces
ΔT
5 nm
50 nm

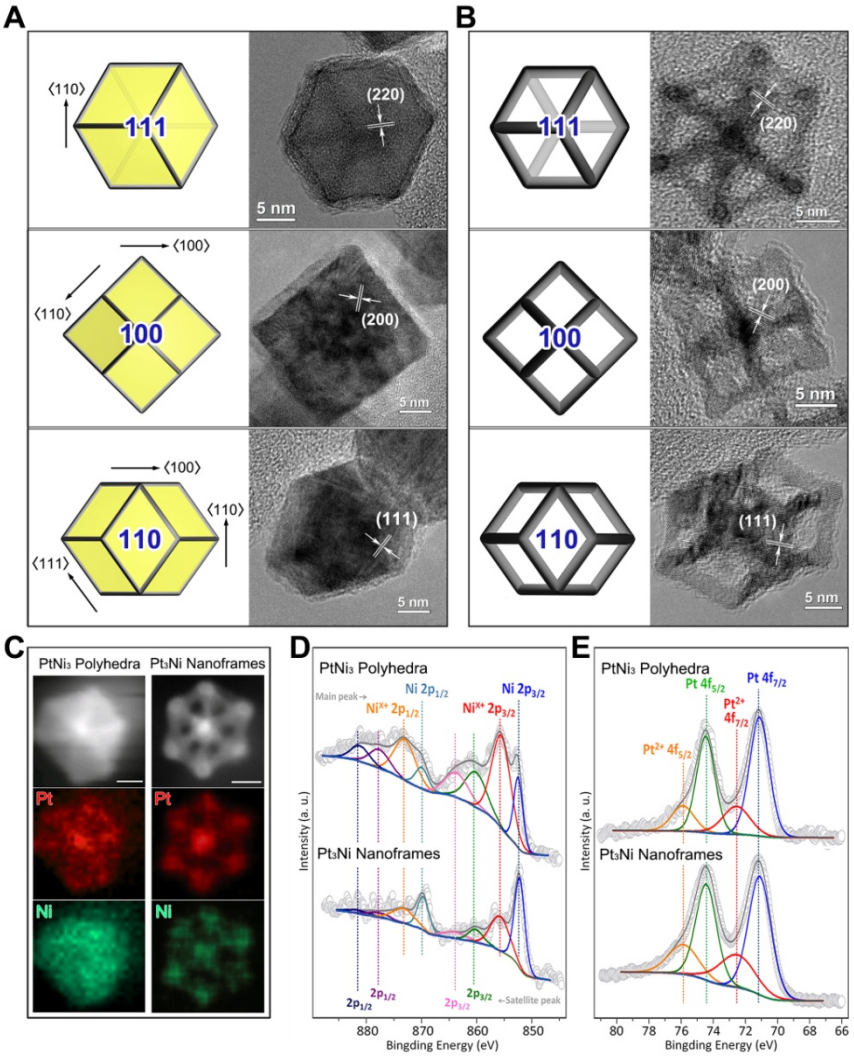

Fig. 2. Electron microscopy characterization of the initial $PtNi_3$ polyhedron and final Pt_3Ni nanoframes: **(A)** Three typical principle projections of the initial $PtNi_3$ polyhedron revealed a morphology of solid rhombic dodecahedron with single crystallinity. **(B)** The final Pt_3Ni nanoframe well inherits the symmetry and single crystallinity of parent $PtNi_3$ polyhedron, with a hollow interior developed and 24 edges (ca. 2 nm in diameter) remaining. For each projection of both initial polyhedron and final frame, the schematic illustration (left), HRTEM image (middle), corresponding FFT pattern (bottom right) and HAADF-STEM image (top right) are shown. Elemental analysis was carried out to support the proposed mechanism responsible for the spontaneous structural evolution. **(C)** EDX elemental mapping results for $PtNi_3$ polyhedron and Pt_3Ni nanoframe, suggesting that, Ni is homogeneously distributed whereas Pt in the parent $PtNi_3$ has a slightly higher ratio on the edges (scale bar, 5 nm). **(D)** Ni 2p and **(E)** Pt 4f XPS spectra of $PtNi_3$ polyhedra and Pt_3Ni nanoframes, from which it can be seen that, during the evolution process, the intensity of Ni^{x+} relative to Ni decreased whereas the relative ratio of Pt^{2+} to Pt is barely changed.

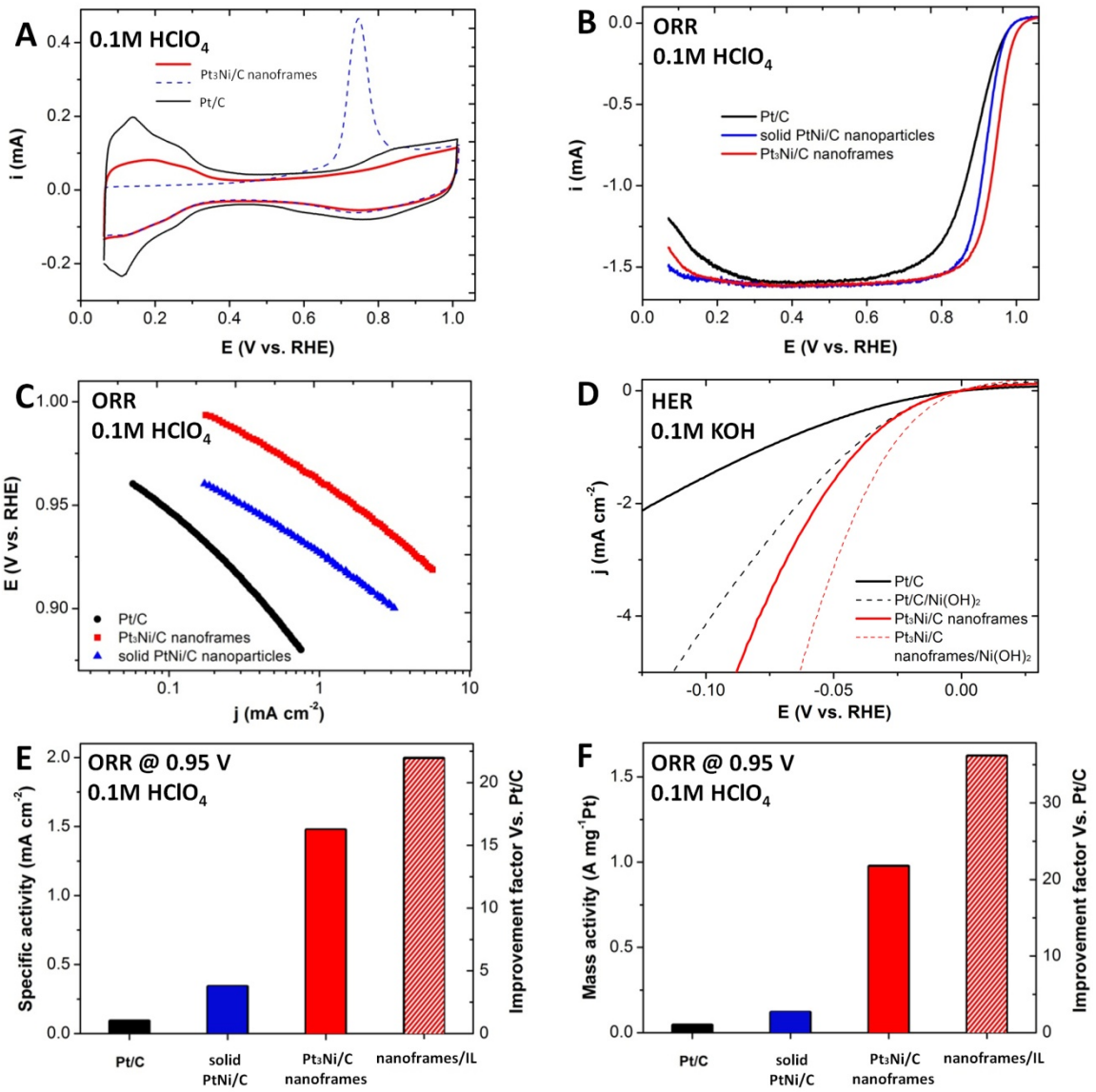

Fig. 3. (A) Cyclic voltammograms of Pt/C and Pt_3Ni/C nanoframes signify the difference in surface coverage by H_{upd} and OH_{ad}. ECSA of the nanoframes is determined by integrated charge of adsorbed CO electrooxidation curve. **(B)** The ORR polarization curves and **(C)** corresponding Tafel plots. **(D)** HER activities for Pt/C, Pt/$Ni(OH)_2$/C, Pt_3Ni nanoframes/C, and Pt_3Ni frames/$Ni(OH)_2$/C in alkaline electrolyte. **(E)** Specific activities and **(F)** mass activities measured at 0.95 V and improvement factors versus Pt/C catalysts. Because of the high intrinsic activity of the Pt_3Ni nanoframes the ORR activity values are given at 0.95 V in order to avoid the extensive error margin introduced by the close proximity of current values at 0.9 V to the diffusion limited current.

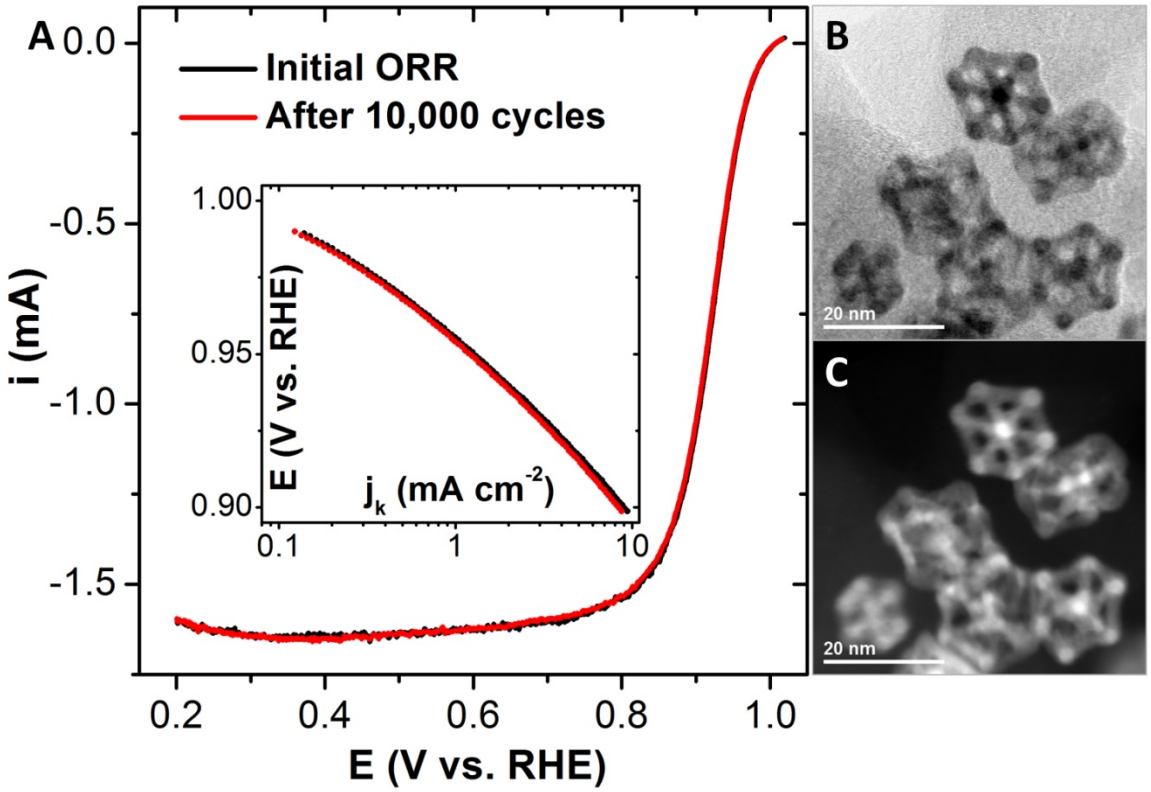

Fig. 4. (A) The ORR polarization curves and (inset) corresponding Tafel plots of Pt_3Ni frames before and after 10,000 cycles. **(B)** Bright-field and **(C)** dark-field STEM images of Pt_3Ni nanoframes/C after cycles.